Multiphoton Phosphorescence Quenching Microscopy Reveals Kinetics of Tumor Oxygenation during Antiangiogenesis and Angiotensin Signaling Inhibition

John D. Martin[1,2], Ryan M. Lanning[1,3], Vikash P. Chauhan[1,4], Margaret R. Martin[1], Ahmed S. Mousa[1], Walid S. Kamoun[1], Hee-Sun Han[5], Hang Lee[6], Triantafyllos Stylianopoulos[1], Moungi G. Bawendi[5], Dan G. Duda[1], Edward B. Brown[1], Timothy P. Padera[1], Dai Fukumura[1], and Rakesh K. Jain[1]

ABSTRACT

Purpose: The abnormal function of tumor blood vessels causes tissue hypoxia, promoting disease progression and treatment resistance. Although tumor microenvironment normalization strategies can alleviate hypoxia globally, how local oxygen levels change is not known because of the inability to longitudinally assess vascular and interstitial oxygen in tumors with sufficient resolution. Understanding the spatial and temporal heterogeneity should help improve the outcome of various normalization strategies.

Experimental Design: We developed a multiphoton phosphorescence quenching microscopy system using a low-molecular-weight palladium porphyrin probe to measure perfused vessels, oxygen tension, and their spatial correlations *in vivo* in mouse skin, bone marrow, and four different tumor models. Further, we measured the temporal and spatial changes in oxygen and vessel perfusion in tumors in response to an anti-VEGFR2 antibody (DC101) and an angiotensin-receptor blocker (losartan).

Results: We found that vessel function was highly dependent on tumor type. Although some tumors had vessels with greater oxygen-carrying ability than those of normal skin, most tumors had inefficient vessels. Further, intervessel heterogeneity in tumors is associated with heterogeneous response to DC101 and losartan. Using both vascular and stromal normalizing agents, we show that spatial heterogeneity in oxygen levels persists, even with reductions in mean extravascular hypoxia.

Conclusions: High-resolution spatial and temporal responses of tumor vessels to two agents known to improve vascular perfusion globally reveal spatially heterogeneous changes in vessel structure and function. These dynamic vascular changes should be considered in optimizing the dose and schedule of vascular and stromal normalizing strategies to improve the therapeutic outcome.

Introduction

Abnormal blood vasculature and the resulting tissue hypoxia constitute hallmarks of malignant tumors and correlate with poor survival in patients with cancer (1, 2). Hypoxia drives tumor progression and promotes/mediates resistance to various treatments including radiation, most chemotherapies, and immunotherapies (1, 2). The imbalance between pro- and antiangiogenic signaling leads to tortuous, dilated, and highly permeable blood vessels, resulting in reduced perfusion and insufficient oxygen delivery (1). Additionally, the expansion of tumors due to uncontrolled cell proliferation and extracellular matrix production within confining surrounding tissue generates a compressive mechanical force (solid stress), which causes the collapse of tumor vessels (3, 4). Vessel compression compromises blood flow (5), leaving intratumoral regions up to 1 mm or larger without blood perfusion (6) and minimal oxygen supply. However, the extent of spatial heterogeneity in the function of tumor vessels and local oxygen concentrations and how they affect treatment response are not well characterized.

When judiciously applied, antiangiogenic therapies (AAT) can prune immature, inefficient tumor vessels and fortify the remaining vessels (7, 8). The net result is "normalization" of vessel permeability and architecture through pericyte recruitment via Ang1/Tie2 signaling as early as 6 hours after AAT administration (9–11). Vascular

[1]Edwin L. Steele Laboratories, Department of Radiation Oncology, Massachusetts General Hospital, Harvard Medical School, Boston, Massachusetts. [2]Department of Chemical Engineering, Massachusetts Institute of Technology, Cambridge, Massachusetts. [3]Harvard-Massachusetts Institute of Technology Division of Health Sciences and Technology, Cambridge, Massachusetts. [4]School of Engineering and Applied Sciences, Harvard University, Cambridge, Massachusetts. [5]Department of Chemistry, Massachusetts Institute of Technology, Cambridge, Massachusetts. [6]Biostatistics Center, Harvard Medical School, Massachusetts General Hospital, Boston, Massachusetts.

Note: Supplementary data for this article are available at Clinical Cancer Research Online (http://clincancerres.aacrjournals.org/).

Current address for John D. Martin: NanoCarrier Co., Ltd., Tokyo, Japan; current address for Ryan M. Lanning: Department of Radiation Oncology, School of Medicine, University of Colorado, Aurora, CO; current address for Vikash P. Chauhan: Koch Institute for Integrative Cancer Research, Massachusetts Institute of Technology, Cambridge, MA; current address for Margaret R. Martin: Department of Computer Science, Tufts University, Medford, MA; current address for Ahmed S. Mousa: Pieris Pharmaceuticals, Inc., Boston, MA; current address for Walid S. Kamoun: Servier Pharma, Boston, MA; current address for Hee-Sun Han: Department of Chemistry, University of Illinois, Urbana, IL; current address for Triantafyllos Stylianopoulos: Cancer Biophysics Laboratory, Department of Mechanical and Manufacturing Engineering, University of Cyprus, Nicosia, Cyprus; and current address for Edward B. Brown: Department of Biomedical Engineering, University of Rochester, Rochester, NY.

J.D. Martin and R.M. Lanning contributed equally to this work.

Corresponding Author: Rakesh K. Jain, Department of Radiation Oncology, 100 Blossom Street, Cox 7, Boston, MA 02114. E-mail: jain@steele.mgh.harvard.edu

Clin Cancer Res 2022;28:3076–90

doi: 10.1158/1078-0432.CCR-22-0486

This open access article is distributed under the Creative Commons Attribution-NonCommercial-NoDerivatives 4.0 International (CC BY-NC-ND 4.0) license.

©2022 The Authors; Published by the American Association for Cancer Research

Downloaded from http://aacrjournals.org/clincancerres/article-pdf/28/14/3076/3186259/3076.pdf by guest on 21 September 2023

Translational Relevance

Abnormal tumor vessels promote tumor progression and treatment resistance. We have developed two approaches to repair tumor blood vessels and improve their function. One approach employs VEGF pathway inhibition, which can restore the balance between pro- and antiangiogenic signaling and transiently "normalize" vascular structure and function resulting in improved tumor blood flow. The second approach utilizes angiotensin system inhibitors (ASI), which can alleviate the compressive forces generated by growing tumors that collapse tumor blood vessels. ASIs decompress tumor blood vessels, thereby restoring blood flow toward alleviating hypoxia and its downstream effects. Using multiphoton microscopy, here we show that although mean extravascular hypoxia in tumors is alleviated with a judicious application of an anti-VEGFR2 antibody or losartan (an ASI), spatial and temporal heterogeneities persist. Moreover, the complementary vascular changes in response to these two approaches suggest a potential for combining them to improve treatment outcomes dependent on oxygenation.

normalization transiently increases perfusion (12–15), oxygen delivery (9, 16), and immune cell infiltration in both murine and human tumors (12, 17). Therefore, increases in tissue perfusion and oxygenation are potential dynamic biomarkers of response to AATs (2, 13, 14, 16). Conversely, AATs administered at high doses and/or for an extended duration can prune vessels excessively and exacerbate hypoxia (1, 2, 9, 18, 19). Separately, AAT cannot reach collapsed, and thus not perfused, vessels in highly desmoplastic tumors (1, 20, 21). In contrast, drugs that kill cancer cells and/or alleviate desmoplasia can decompress vessels in these hypoperfused tumors (5, 22, 23). For instance, angiotensin-receptor blockers (ARB), such as losartan, have antifibrotic properties in tumors by reducing transforming growth factor (TGF)-β1 activation (24) by antagonizing the angiotensin-II-receptor-1 on cancer-associated fibroblasts (5). As a result, ARBs decompress and normalize blood vessels in a variety of tumor models (5, 25, 26). However, the spatiotemporal dynamics and heterogeneity of these processes at cellular resolution are unknown.

To address this unmet need, we developed a multiphoton (MP) phosphorescence quenching microscopy (PQM) method (MP-PQM). MP microscopy enables visualization of perfused vessels in tumor models propagated in mice with micron resolution (27). Meanwhile, PQM allows direct measurements of tissue oxygenation based on the interaction of surrounding molecular oxygen with the light-excited triplet state of a phosphorescent reporter molecule. We have previously used intravital PQM with conventional and confocal fluorescence microscopy to measure tissue oxygen levels (28, 29). However, these approaches can cause photodamage and have limited three-dimensional resolution (28). Existing PQM for MP microscopy techniques use high-molecular-weight probes that are confined to the vasculature following intravenous administration (30). These nano-sized probes might have difficulty distributing uniformly throughout tumor extracellular space even with an intratumor injection. Here, we use a low-molecular-weight palladium porphyrin probe that is able to (i) distribute throughout the tumor and (ii) extravasate into tissues from sinusoidal, reticuloendothelial vessels, such as those in bone marrow, when injected intravenously (31). This probe along with MP-PQM allowed us to measure oxygen tension (pO_2) in normal tissues and breast cancers in mice as well as the spatial heterogeneity in the vessel and pO_2 response to AAT and ARBs. Our measurements reveal spatially heterogeneous changes in vessel structure and function in response to AAT, presumably due to the heterogeneities in the local imbalance of pro- and antiangiogenic signaling. In contrast, losartan, an ARB, increased perfused vessel density—as expected—and increased oxygen delivery.

Materials and Methods

Multiphoton PQM system

We custom-modified a multiphoton microscope based on the Fluoview 300 laser scanner (Olympus FV300, Optical Analysis) and upright microscope (Olympus BX61WI Optical Analysis) incorporating a broadband (710–1,020 nm) Ti:Sapphire femtosecond laser (MaiTai HP, Spectraphysics) as the excitation source. The output power of the laser was adjusted by a zero-order half-wave plate (10RP52-2, Newport Corp.) and Glan-Laser polarizer (10GL08AR.16, Newport Corp.). For PQM, we used a KD*P Pockels cell (Model: 350-50; Conoptics, Inc.) electro-optic modulator driven by custom-built electronics to amplify triggering pulses from a digital delay generator (DG535, SRS) as a temporal gate. Excitation pulse selection was placed immediately prior to beam expansion which fed the laser into the galvanometer-based scanner. Based on the *in vitro* or biological system (tissue) in which pO_2 measurements were performed, the excitation pulse for MP-PQM ranged from 1.28 to 15.36 μs. Focusing and collecting light was performed with a 20×, 0.95 NA water immersion objective lens (Olympus XLUMPlanFl, Optical Analysis). Given the short spectral separation between the long emission of the phosphorescent sensors (∼690 nm) and the excitation laser wavelength, a short-pass (<750 nm) AR-coated filter was used in the detector path (750SP-2P, Chroma Technology Corp.) to limit background counts from the laser. A 690/90 bandpass filter (690/90M, Chroma Technology Corp.), and focusing lens were used before the detectors (GaAs photomultiplier tube for *in vivo* measurements: H7421-50, Hamamatsu, Inc.; or a silicon avalanche photodiode detector for *in vitro* measurements: SPCM-AQR-12-FC, PerkinElmer). For time-domain photon counting, we used a multichannel scaler (SR430, SRS). PQM measurements were performed using a stationary beam with sample scanning performed by an automated mechanized XY stage (H101; Prior Scientific). A custom-designed graphical user interface programmed in LabView (National Instruments; RRID:SCR_014325) was used for data acquisition and processing with embedded MATLAB fitting algorithms (MathWorks; RRID:SCR_001622).

Characterization and calibration of oxyphor R2 for MP-PQM

We obtained the soluble phosphorescent oxygen sensor Pd-meso-tetra-(4-carboxyphenyl) porphyrin dendrimer from commercial sources (OxyphorR2, Oxygen Enterprises, Ltd.). We determined the ideal multiphoton excitation wavelength by measuring the single-photon excitation spectrum using a spectrophotometer (Beckham Instruments Inc.) with continuous illumination from 400 to 1,000 nm and the two-photon excitation spectrum by measuring the photon counts after time-domain pulsed excitation from 800 to 1020 nm at constant laser power. We confirmed that phosphorescence saturation did not occur within our selected excitation pulse duration. For the calibration of Oxyphor R2, we custom designed a sealed recirculating system using a fiber oxygenator to equilibrate the circulating fluid with gas mixtures of known oxygen concentration balanced with nitrogen. The oxygen tension in the calibration solution was independently measured using a fiber optic ruthenium-based sensor (FOXY, Ocean Optics, Inc.). All tubing in the system was impermeable to oxygen

Downloaded from http://aacrjournals.org/clincancerres/article-pdf/28/14/3076/3186259/3076.pdf by guest on 21 September 2023

(Tygon PVC, McMaster-Carr Supply Co.). A solution of 1 mg/mL (3.6 × 10–4 M) OxyphorR2 in PBS at pH 7.4 was equilibrated with known nitrogen gas mixtures of 0, 1, 2, 5, 10% oxygen (0–80 mm Hg) and various concentrations of BSA (BSA) from 0 to 10% using the fiber oxygenator (Hemophan Membrane Fiber Oxygenator, Harvard Apparatus). After equilibration with the applied gas mixture, the solution was passed through an oxygen impermeable spectrophotometer flow cell with 500-μm thick walls (45-Q-2, Starna Cells, Inc.). MP-PQM calibration measurements were performed within the flow cell at 37°C. To measure the anoxic phosphorescence lifetime (τ_0) measurements, we used a Schlenk-line freeze-pump thaw method to create deoxygenated solutions in 10-mm pathlength quartz cuvettes with a vapor pressure of 10^{-6} Torr. Using an unconstrained nonlinear optimization in MATLAB, we fit the phosphorescence decays to a two-component Stern-Volmer model due to binding of the oxygen sensor to proteins creating two species with different luminescent lifetimes.

Animal studies

All animal experimental protocols were reviewed and approved by the Institutional Animal Care and Use Committee. The dorsal skinfold chamber, mammary fat pad window, and chronic bone marrow chamber models were prepared in SCID mice as previously described (32, 33). For the breast tumor experiments, the appropriate tumor type was implanted as a single-cell suspension or homogenized tumor tissue from an existing xenograft in the center of the mammary fat pad chamber 2 to 3 days after the initial surgery. The murine mammary adenocarcinomas MCaIV and E0771 (CH3 BioSystems) were transplanted from subcutaneous tumors grown in syngeneic mice. Cranial window chamber models were prepared in nude mice as previously described (34). The mice were allowed to recover for one week following the procedure. U87 (ATCC) fragments up to 0.3 mm in diameter dissected from tumors excised growing in a source mouse were implanted in the left cerebral hemisphere 0.5 to 1.0 mm deep. Animals were anesthetized with Ketamine/Xylazine (90/9 mg/kg) for surgeries and isoflurane (1%–3% in medical-grade air) for all imaging experiments. The cells were tested and authenticated by *mycoplasma* testing, morphology using microscopy and binding of antibodies for common viral contaminations (VRL Diagnostics) after thawing cells to inoculate into source mice. Tumors were implanted usually after three but no more than five passages.

Fifteen minutes prior to MP-PQM measurements, the animal was anesthetized by isoflurane (3% for the first 4 minutes) in medical air carrier gas. This method of anesthesia was selected given its neutrality toward heart rate, blood pressure, and oxygen tension (35–37), particularly compared with other methods that alter oxygen tension (28, 35). Immediately following isoflurane induction, a mixture (200 μL) of 10 mg/mL Oxyphor R2 with 8 mg/mL 2M MW FITC-dextran was injected intravenously through the retro-orbital route. With animals under isoflurane anesthesia, we secured the frame of the transparent window or secured the skull to prevent motion artifacts during imaging. This allows both real-time measurements of pO_2 and intravital high-resolution fluorescent angiography. For oxygen tension maps, we manually selected a rectangular region of interest and collected an automated series of mosaic multiphoton microscopy images covering the ROI. Each image contained an axial series up to 400 μm deep in the tissue at a 5-μm z-step size. Following angiography imaging, MP-PQM measurements were performed as a series of 144 stationary points based on a 12 × 12 grid covering the ROI at four equally spaced depth planes. Total data collection times ranged from two to three hours depending upon the size of the ROI. Anesthesia was maintained at 1% isoflurane in a normoxic (21% FiO_2) atmospheric mixture with a circulating water heating pad maintaining the animal's body temperature at 37°C. Animals were monitored for any movement using a remote digital camera. To account for evaporation of water at the interface of the water-immersion objective lens with the window chamber, a syringe pump was utilized to slowly apply distilled water to the top of the chamber.

Antiangiogenic VEGFR2 blockade treatments with DC101, a monoclonal antibody against murine VEGFR2 (Eli Lilly and Company), or nonspecific rat IgG were administered intraperitoneally at 40 mg/kg as prescribed in previous studies (24) or at 5 mg/kg for low AAT dose studies (33). We gave three doses of DC101 at three-day intervals (days 0, 3, and 6) with MP-PQM performed the day immediately prior to each treatment. Imaging was performed through day 8. Therapeutic initiation was determined through monitoring of tumor growth by visual inspection of the enface tumor diameter (≥4 mm) and angiogenesis of the tumor (vascularized throughout).

To replicate the conditions of our previous work (5), losartan was obtained as pills intended for clinical use from the Massachusetts General Hospital Pharmacy, crushed and dissolved in PBS for 24 hours. The solutions were then sterile filtered for injection. The concentration of the active ingredient was not confirmed before administration, and it was assumed that no active pharmaceutical ingredient was lost in this process when calculating the doses administered. The mice were treated with 40 mg/kg losartan or an equal volume of PBS intraperitoneally every day for 6 days.

Data analysis

We developed a custom code in MATLAB to process and analyze the *in vivo* MPM angiography images. Colorized depth projections were created to display the vascular networks in conjunction with the oxygen tension measurements. A semiautomated vascular tracing method previously reported by our group (25, 26) was applied to the mosaic image of the entire ROI. Briefly, this method uses an algorithm that models vascular segments as superellipsoids to obtain three-dimensional trajectories and morphology of the individual segments of the vascular network. The output of the tracing algorithm was correlated with each individual oxygen measurement to quantify distance to nearest vessel and diameter of that vessel. Phosphorescence lifetimes were determined by fitting a two-component exponential decay model with oxygen tension values calculated using the Stern–Volmer relationship and the quenching constant and anoxic lifetime determined from *in vitro* calibrations. Oxygen tension maps were created in MATLAB using custom code to overlay the mesh grid of pO_2 values with outlines of the vascular tracing. Mean oxygen tension was calculated from the pool of all the measurements for each individual tumor. We determined tumor oxygen profiles using a sliding averaging procedure. For each tumor type, the distributions are a collection of all tumors imaged at that timepoint or within a specific treatment group. Measurements classified as interstitial or extravascular oxygenation occurred between 40 and 60 μm from the nearest vessel.

Statistical analysis

Data are reported as mean ± standard error of the mean (SEM). For experiments involving ensemble statistics, significant differences between groups were determined using a Kruskal–Wallis test correcting for multiple comparisons using Dunn's correction (Prism, GraphPad Software, LLC., RRID:SCR_002798), because the distributions were not normally distributed. To rule out type I error inflation in statistically significant comparisons between control and treatment groups from the same study day (e.g., DC101 treatment on day 2), Bonferroni's correction was applied, which involved multiplying the

Downloaded from http://aacrjournals.org/clincancerres/article-pdf/28/14/3076/3186259/3076.pdf by guest on 21 September 2023

Mann–Whitney *U* test (obtained in Prism) *P* value by the number of comparisons in the Kruskal–Wallis test (i.e., 15) and setting $P < 0.05$ as the threshold for statistical significance. For experiments involving ensemble statistics that investigated treatment response over time, general linear models (obtained in Prism) were applied to assess the time × treatment interaction on intravascular and extravascular oxygenation. In experiments involving comparisons between two groups, statistical significance was tested using an unpaired, two-sided Student *t* test. All correlations were determined using the Pearson product–moment correlation. $P < 0.05$ was considered statistically significant for all comparisons except for the test with Bonferroni's correction, in which $P < 0.05$ was used.

Data availability

The data generated in this study are available within the article and its supplementary data files.

Results

Oxygen probe and system characterization

We constructed a custom MP-PQM system for the quantification of pO_2 *in vitro* and *in vivo* (**Fig. 1A**). To maximize signal-to-noise ratio *in vivo*, we measured phosphorescence lifetime in the time domain (38) utilizing an electro-optic modulator to gate pulses of the femtosecond excitation laser at a stationary location with sample scanning performed by a programmable XY stage. Palladium porphyrin has longer lifetimes than platinum porphyrin, thereby making the signal easier to detect (39). The two-photon action cross-section of Pd-porphyrin molecules, similar to the one we used here, is known to be below 6 Goppart-Meyer (40). Thus, we measured the single- and two-photon action cross-sections in order to determine the ideal excitation wavelength balancing (i) minimal overlap with the single-photon excitation or phosphorescence emission and (ii) maximal excitation/emission efficiency (**Fig. 1B**). We selected the nonlinear excitation at 1,020 nm rather than at 800 nm to limit cellular damage, reduce tissue scattering allowing for deeper measurements, and avoid overlap with the phosphorescence emission, which extends to 780 nm. Nonlinear, two-photon excitation of the Pd-porphyrin probe was confirmed at the selected excitation wavelength of 1,020 nm and was independent of oxygen tension (**Fig. 1C**). This relationship held *in vivo*, which confirmed that excitation of the Pd-porphyrin probe at 1,020 nm is a two-photon excitation process in our system (**Fig. 1D**). Finally, we calibrated the phosphorescence lifetime of the Pd-porphyrin probe at various levels of pO_2 in solutions with differing concentrations of BSA using a customized calibration system (**Fig. 1E**). Given two states of the probe (free in solution or bound to protein), the best fit was to a two-component Stern–Volmer model (**Fig. 1F**; ref. 41). Adding fluorescent quantum dots to the solution did not affect the calibration indicating that adding other fluorescent species into the same sample does not affect the measurements (Supplementary Fig. S1). Variability increased with oxygenation because the phosphorescence lifetime is shorter with higher oxygen tension (Supplementary Fig. S2). Measuring in the time domain, the technical maximum oxygen measurement limit of the system is a pO_2 of 122 mm Hg because the minimum phosphorescence signal collection time of our system is 2.56 μs.

Oxygen delivery by blood vessels in normal skin and bone marrow

We next measured perfused vessel morphology and interstitial oxygen in the skin of mice breathing air (**Fig. 2A** and **B**), the skin of mice breathing 100% oxygen (**Fig. 2C** and **D**), and the bone marrow of mice breathing air (Supplementary Fig. S3). Throughout the skin, extravascular regions were an average of 25 μm from the nearest perfused vessel and at most 84 μm away (Supplementary Table S1). Throughout the bone marrow, which has sinusoidal vessels hyperpermeable to BSA (Supplementary Fig. S4), extravascular regions were an average of 13 μm from the nearest perfused vessel and at most 58 μm away (Supplementary Table S1). These maximum distances are less than 150 μm from perfused vessels, which is considered the maximum diffusible distance of oxygen due to oxygen consumption (6, 29).

Typically, larger diameter vessels have higher blood flow rates than smaller vessels (e.g., capillaries <10 μm, arteries and venules >10 μm), and, thus, we hypothesized that larger vessels can deliver oxygen at a higher rate to surrounding tissues (42). To test this hypothesis, we imaged perfused vessels using a fluorescent vascular tracer and measured oxygen content over a large region of tissue (2.5 × 2.5 mm). Within the dorsal skinfold chamber, there was a direct and statistically significant Pearson product–moment correlation (i.e., coefficient greater than 0.00 and $P < 0.05$) of 0.326 between vessel diameter and interstitial oxygenation (i.e., measured at 40 to 60 μm from the nearest vessel), indicating that larger vessels supply more oxygen to the extravascular space (**Fig. 2A**, **B**, and **E**). Some large vessels above 90 μm diameter—likely venules—had low surrounding interstitial oxygen, which resulted in no correlation between vessel diameter and oxygen when considering the largest vessels only (**Fig. 2B**). When the same mice were subsequently placed under hyperoxic conditions (100% inspired oxygen), the average intravascular oxygen tension increased from 42 to 80 mm Hg, and the correlation between vessel diameter and interstitial oxygenation remained statistically significant (**Fig. 2C–E**). Again, we found no correlation for large vessels with diameters larger than 90 μm (**Fig. 2D**). In the bone marrow cavities of the mouse calvarium that contained multiple vessels (Supplementary Fig. S3A and S3B) and in the cellular areas surrounding single endosteal vessels (Supplementary Fig. S3C and S3D), there was also a correlation between vessel diameter and interstitial oxygen (**Fig. 2E**). Thus, in murine skin and bone marrow, there is a direct correlation of interstitial oxygenation and the diameter of the nearest perfused capillary.

As oxygen diffuses radially through the vessel wall and away from vessels, it is consumed by cells and the concentration falls with increasing distance from the vessel (29). Nonetheless, oxygen tension levels are highly regulated to ensure that even cells farthest from blood vessels have sufficient oxygenation. As such, we observed in the skin a weak although statistically significant inverse correlation (i.e., coefficient less than 0.00 and $P < 0.05$) of –0.119 between extravascular oxygenation and distance from the nearest vessel (**Fig. 2F**). However, we were unable to analyze our data for a correlation between extravascular oxygenation and distance from the nearest vessel when the same mice were subsequently placed under hyperoxic conditions because the measurement technique is constrained by an upper limit of 122 mm Hg oxygen tension (**Fig. 2G** and **H**). In the bone marrow cavities of the mouse calvarium containing multiple vessels, no correlation between oxygen and distance from the nearest vessel was found (**Fig. 2H**; Supplementary Fig. S3). This is because there are many vessels near each other, even tissue areas relatively far from a given vessel still have other vessels in close proximity (Supplementary Table S1) that could contribute to the oxygen supply. In contrast, the cellular areas surrounding single endosteal vessels surrounded by bone maintained a statistically significant inverse relationship between oxygenation and distance from the vessel (**Fig. 2H**), consistent with a previous report (31). Thus, in murine skin and bone, there is a weak

Downloaded from http://aacrjournals.org/clincancerres/article-pdf/28/14/3076/3186259/3076.pdf by guest on 21 September 2023

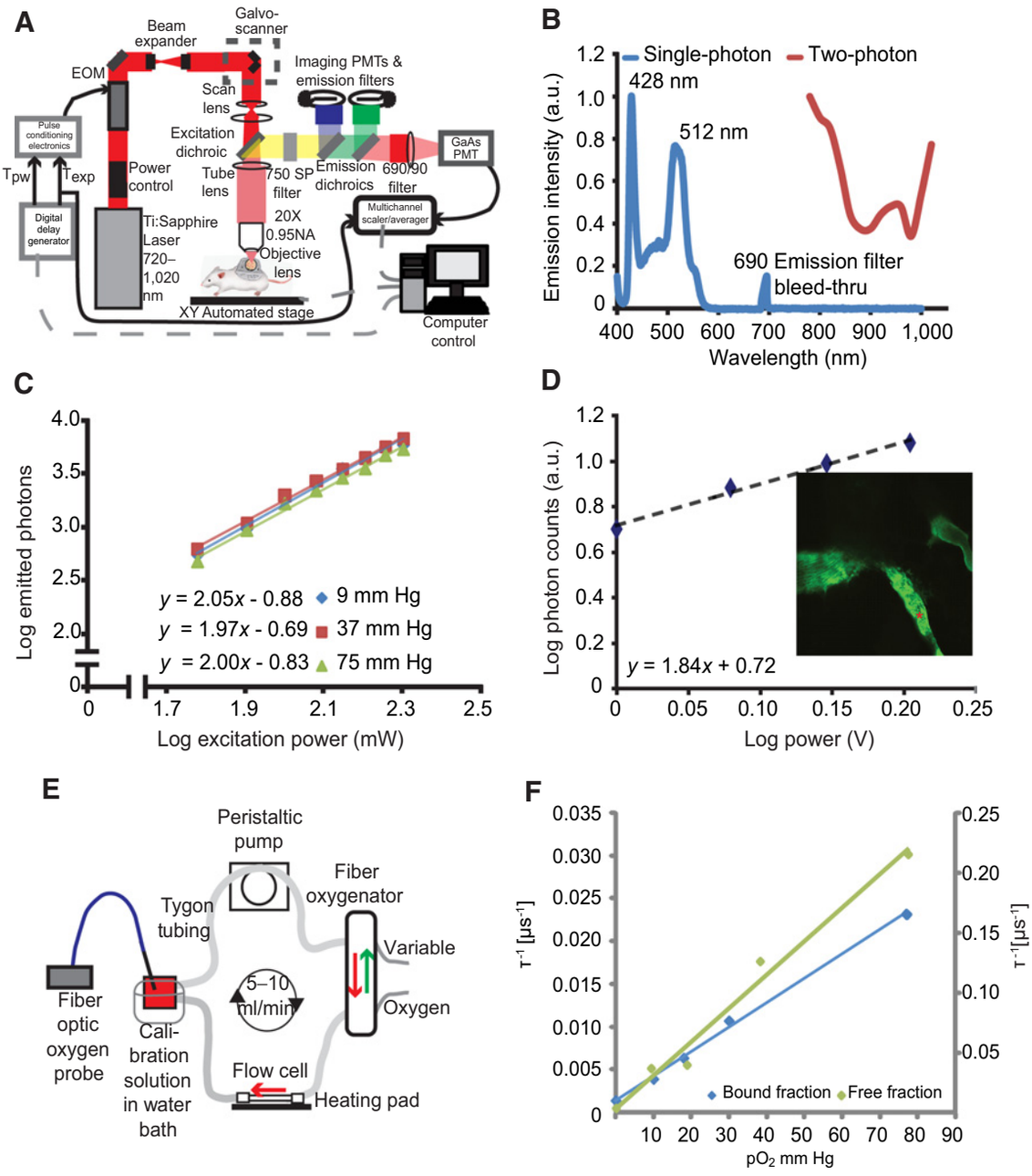

Figure 1.

Multiphoton phosphorescence quenching microscopy (MP-PQM). **A,** Schematic of the experimental setup. EOM, electro-optic multiplier; PMTs, photomultiplier tubes; GaAs, Gallium arsenide; T_{pw}, temporal duration of the excitation pulse width; T_{exp}, duration of the experimental triggering time. Arrows indicate the direction of communication. Dashed gray lines indicate two-way communication. **B,** Single- and two-photon action cross-sections for Pd-porphyrin soluble oxygen sensor. The single-photon excitation spectrum (blue line) does not show absorption or emission in the wavelength range of two-photon (red line). The lone peak at 690 nm is due to excitation light at the same wavelength as the emission bandpass filter in the spectrophotometer. **C,** Two-photon excitation at 1,020 nm of Pd-porphyrin phosphorescent oxygen sensor relating the emitted photons to the excitation power on a log–log scale. The experiment was repeated at oxygen tensions of 9 mm Hg, 37 mm Hg, and 75 mm Hg (blue, red, and green lines, respectively). **D,** In vivo two-photon excitation of Pd-porphyrin oxygen sensor. A series of time-domain lifetime measurements performed in tumor vasculature (red asterisk, inset) shows the nonlinear excitation of the Pd-porphyrin sensor. **E,** Diagram of the recirculating, sealed calibration system using a fiber oxygenator indicating the direction of fluid and gas flow. An independent pO_2 measurement is made with a calibrated optical fiber ruthenium-based probe. **F,** Two-photon calibration of the albumin-bound (blue line) and single-component (green line) fits of the Pd-porphyrin oxygen sensor. The left vertical axis applies to the bound fraction. The right vertical axis applies to the free fraction. The vertical axes are the phosphorescence lifetime in units of per μs and the horizontal axis is oxygen tension in units of mm Hg. The Stern–Volmer constant is 3,115 per mm Hg/s for the free fraction and 285 per mm Hg/s for the bound fraction.

Downloaded from http://aacrjournals.org/clincancerres/article-pdf/28/14/3076/3186259/3076.pdf by guest on 21 September 2023

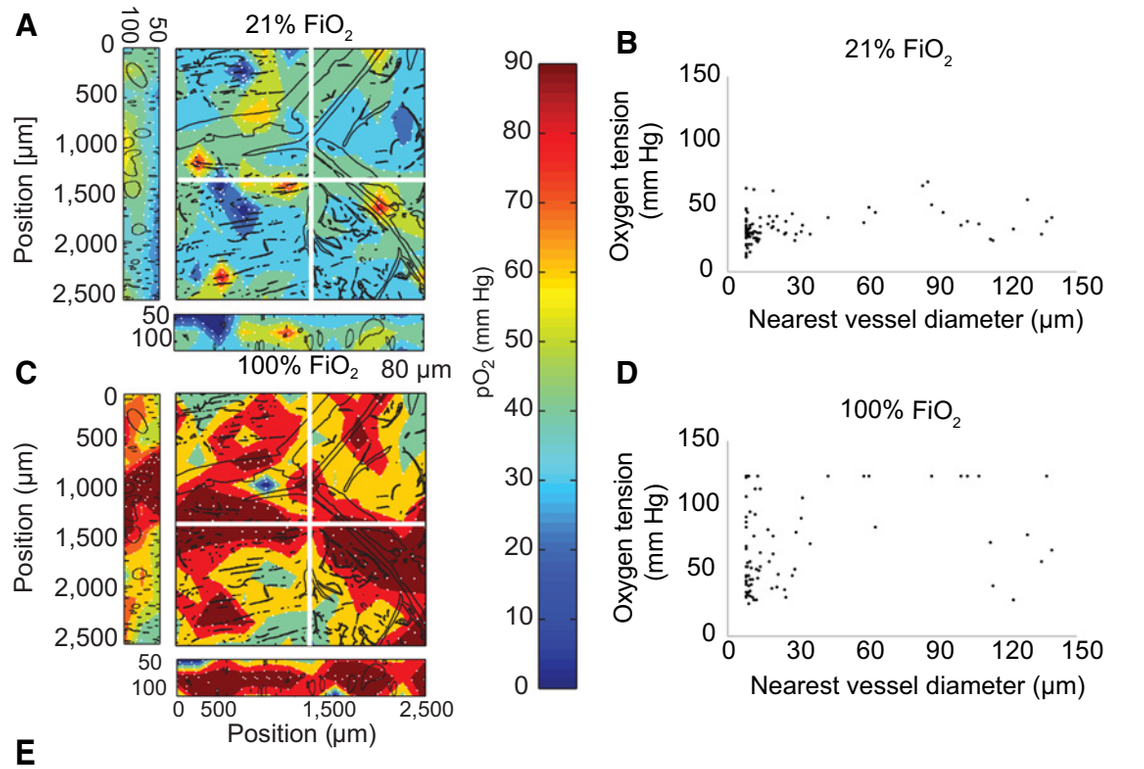

E

Correlation of pO_2 and diameter	Skin–mice breathing air	Skin–mice breathing 100% O_2	Bone marrow single-vessel cavities	Bone marrow endosteal regions
Coefficient	0.326	0.298	0.216	0.143
P value	0.0012	0.007	7.6E-04	0.009

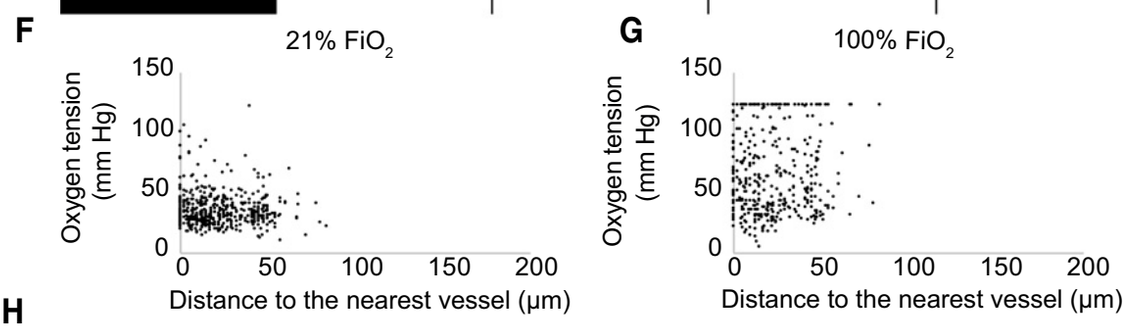

H

Correlation of pO_2 and distance	Skin–mice breathing air	Skin–mice breathing 100% O_2	Bone marrow single vessel cavities	Bone marrow endosteal regions
Coefficient	–0.119	0.0106	0.0667	–0.328
P value	0.0012	0.83	0.30	9.1E-10

Figure 2.

Measurement of pO_2 in mouse tissues. **A,** Oxygen tension map in the normal murine skin of a mouse breathing air (21% oxygen). The depth projection of vasculature (black lines) is overlaid. **B,** Scatter plot of interstitial oxygen tension [mm Hg] versus the diameter of the nearest vessel (μm) in mice breathing air. **C,** Oxygen tension depth projection map in the normal murine skin of a mouse breathing 100% oxygen. **D,** Scatter plot of interstitial oxygen tension versus the diameter of the nearest vessel in mice breathing 100% oxygen. The detection limit of 122 mm Hg is apparent in the data. **E,** Table of Pearson correlation coefficients and the *P* value of the correlation of oxygen tension and nearest vessel diameter. **F,** Scatter plot of measured oxygen tension versus the distance to the nearest vessel in the skin of mice breathing 21% oxygen. **G,** Scatter plot of measured oxygen tension versus the distance to the nearest vessel in the skin of mice breathing 100% oxygen. The detection limit of 122 mm Hg is apparent in the data. **H,** Table of Pearson correlation coefficients, and the *P* value of the correlation of oxygen tension and distance to the nearest vessel.

Downloaded from http://aacrjournals.org/clincancerres/article-pdf/28/14/3076/3186259/3076.pdf by guest on 21 September 2023

inverse correlation between oxygenation and distance to the nearest vessel, except in certain highly vascularized areas.

Oxygen delivery by tumor vessels

Although the vessels in normal tissues are well-organized and function effectively (Supplementary Fig. S5A), tumor vessels are disorganized and dysfunctional (Supplementary Fig. S5B). We next sought to compare tumor blood vessels from four different tumor models with those in normal tissues using MP angiography (Supplementary Fig. S6) and PQM at four tissue depths (**Fig. 3A** and **B**). Unlike vessels in normal tissue, the diameters of tumor vessels do not usually correlate with their function (42). Indeed, of all tumors assessed (Supplementary Fig. S7A), only MCaIV, which is a highly vascularized breast tumor with some large avascular spaces (**Fig. 3C**), exhibited a weak yet statistically significant correlation between vessel diameter and interstitial oxygen tension (**Fig. 3D**; Supplementary Fig. S7A; Supplementary Discussion). This correlation was not seen in hypoperfused tumors, including E0771 murine mammary carcinomas that contain large unperfused regions (**Fig. 3E**), U87 human gliomas, and LS174T human colon carcinomas (**Fig. 3F**; Supplementary Fig. S7A). Thus, in most tumors, the size of the nearest blood vessel did not correlate with the interstitial oxygen tension.

The tumor microenvironment is highly heterogeneous and varies from one tumor to next. Thus, we used four tumor models to compare intravascular oxygen tension measurements. In terms of supply, only LS174T blood vessels had a lower mean intravascular pO_2 than normal skin at room air (**Fig. 3G**). In contrast, MCaIV and U87 tumor blood vessels had 31% and 8% higher intravascular pO_2 than vessels in normal skin, which differed in range but not mean from E0771 (**Fig. 3G**). Although tumors did not consistently have a limited supply of oxygen, highly oxygenated MCaIV and U87 tumor blood vessels did not result in elevated oxygen in the interstitial space (i.e., 40–60 μm from the nearest perfused vessel) compared with normal skin, which we observed as a lower ratio of extravascular (i.e., measurements 40–60 μm from the nearest vessel) to intravascular oxygen tension (**Fig. 3H**). The lower ratio could be a result of high oxygen consumption in tumors by stromal and cancer cells. Our data further show that the oxygen supply in tumor blood vessels is heterogeneous across tumor types and within tumors. Similarly, the efficiency of vessels—defined here as the ratio of extravascular to intravascular oxygen tension—is heterogeneous across tumor types and within a single tumor type compared with vessels of the normal skin.

Next, we investigated how oxygen diffuses from vessels and is consumed by creating scatter plots of oxygen tension as a function of distance to the nearest vessel (Supplementary Fig. S7B and S7C). Like in normal skin, all tumors except the orthotopic glioblastoma U87, which was imaged through an implanted cranial window, had a weak yet statistically significant inverse correlation between distance from the nearest vessel and tissue oxygenation (Supplementary Fig. S7D). This inverse correlation is consistent with our previous report of other tumor models (29). Unlike the hierarchical vascular networks in normal tissues (arteriole to capillary to venule), tumors often have large avascular regions that are too far from vessels for oxygen to diffuse (6). Indeed, in these tumor models, the mean and maximum distances to nearest vessels were around 2–4 times larger than that in normal skin and bone marrow, respectively (Supplementary Fig. S7B and S7C; Supplementary Tables S1 and S2). Orthotopic U87 glioblastoma model, although hypoxic (9), was an exception in regard to distance to a nearest vessel, with high vascularization (43) leaving little extravascular space, as evidenced by the lowest average distance to a vessel among the tumors studied (Supplementary Table S2). Oxygen thus has short distances to diffuse and tissue oxygen could be supplied by multiple vessels, allowing oxygen to distribute relatively evenly, which is indicated by the lack of a correlation between oxygen tension and distance to the nearest vessel (Supplementary Fig. S7D). This constant level of oxygenation in U87 gliomas mirrors that of the normal brain. Thus, like in the skin, oxygen tension fell as a function of distance from the nearest perfused vessels in the tumor models assayed except for orthotopic glioblastoma.

AAT enhances individual vessel function in MCaIV and restores perfusion

Next, we longitudinally measured the density of perfused vessels (Supplementary Fig. S8) and oxygenation (Supplementary Fig. S9) in growing tumors. We then investigated the effect of AAT on tumor vessel pruning and function in two different orthotopic models of murine breast cancer, MCaIV and E0771. Although both tumor models have similar vascular permeabilities (44), MCaIV vessels have larger diameters, interendothelial gaps and intraendothelial holes (~1.5 μm; ref. 45). MCaIV blood vessels have greater intravascular oxygen tension yet are less efficient in delivering oxygen to the interstitial space compared with vessels in normal skin (**Fig. 3G** and **H**). In contrast, E0771 vessels are compressed and hypoperfused owing to increased desmoplasia (5, 46). The oxygen delivery efficiency of E0771 vessels is similar to normal skin albeit with more variability (**Fig. 3H**).

We first monitored oxygenation in MCaIV tumors during two cycles of DC101—a blocking antibody against murine VEGFR2—given i.p. at 40 mg/kg every three days (**Fig. 4A**). We found the intravascular oxygenation in treated tumors decreased with the growth of tumors, and there was no difference between DC101-treated tumors and control IgG-treated ones (**Fig. 4B**). However, extravascular oxygenation—which also decreased with tumor growth (**Fig. 4C**)—was 35% higher on day 2 with DC101 treatment compared with control IgG treatment. This is not surprising as anti-VEGF antibody treatment decreases vessel permeability within six hours thereby causing a transient increase in blood flow and oxygenation (11). The extravascular oxygenation of DC101-treated tumors fell to levels in IgG-treated tumors by day 5 (**Fig. 4C**). Multiple linear regression analysis revealed that extravascular oxygenation in both groups decreased over time ($P < 0.0001$), and the treatment did not affect the overall oxygenation average. However, the rate of decrease per day varied, with the control group's extravascular oxygenation reducing at a rate of 2.8 mm Hg/day ($P < 0.0001$ compared with no change over time) whereas that of the treatment group reduced at a smaller rate of 1.7 mm Hg/day ($P < 0.0241$ compared with the control group's rate; Supplementary Table S3). Consistent with the greater extravascular oxygenation on day 2 in DC101 tumors compared with controls, the efficiency of vessels as measured by the ratio of extravascular oxygen tension to intravascular tension was 23% greater (**Fig. 4D**). At this dose, DC101 reduced the mean extravascular distance to the nearest vessel compared with control on day 2 by 38% and on day 5 by 65% (**Fig. 4E**), suggesting restored perfusion resulting from the increased efficiency of blood flow in MCaIV tumors. Thus, in MCaIV, DC101 at 40 mg/kg normalized tumor vessel function on day 2 and reduced the distance between perfused vessels on days 2 and 5.

AAT induces widespread pruning in E0771

We next investigated DC101 at the same dose (40 mg/kg every 3 days) using the E0771 breast tumor model (**Fig. 5A**), which only requires a lower dose of DC101 to normalize vessel function as measured by an increased rate of extravasation of small

Downloaded from http://aacrjournals.org/clincancerres/article-pdf/28/14/3076/3186259/3076.pdf by guest on 21 September 2023

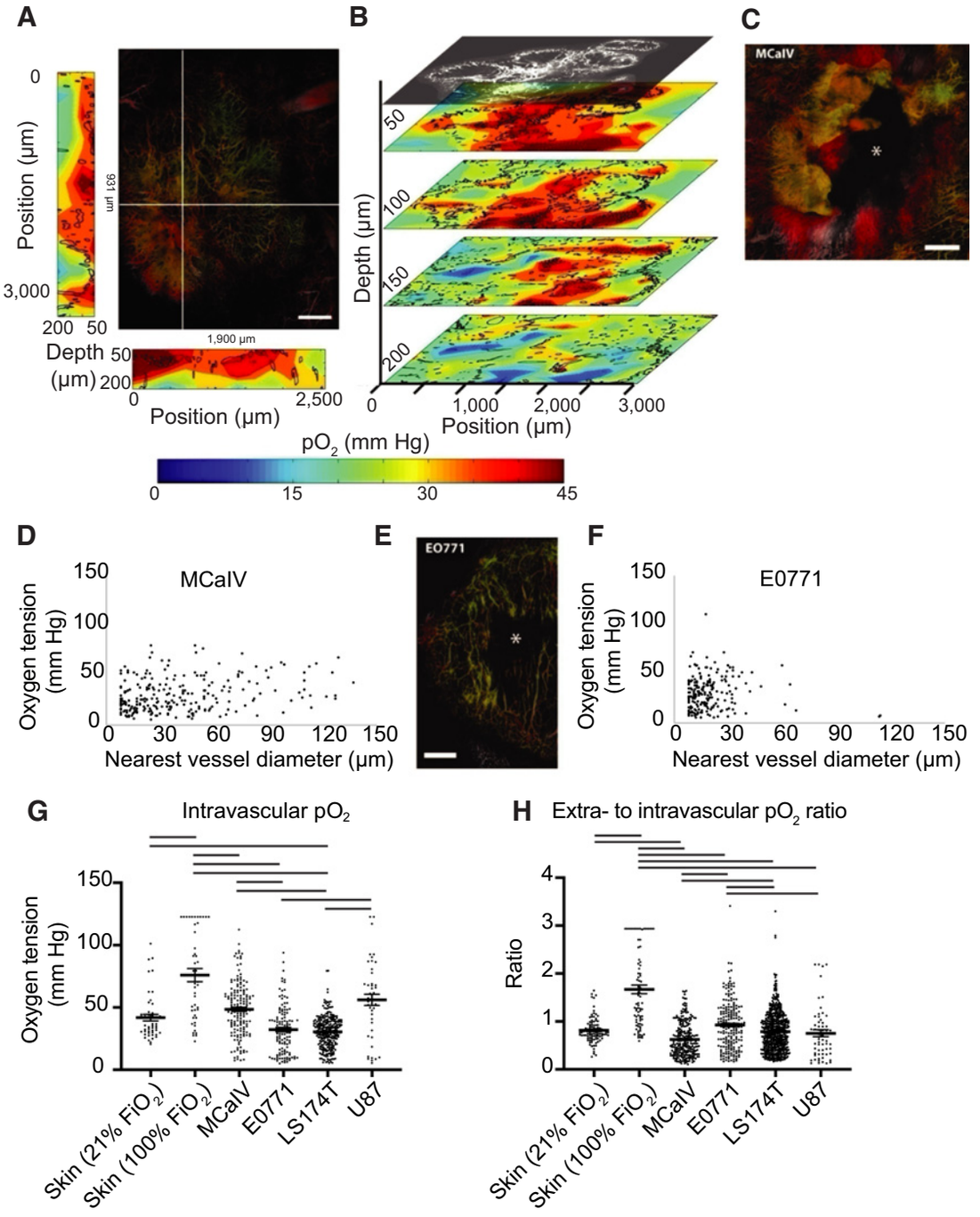

Figure 3.

Simultaneous angiography and oxygen tension measurements reveal an abnormal function of tumor vessels and the dependence of oxygen tension on the distance to the nearest vessel. **A,** The large panel shows a maximum intensity depth projection of MCaIV tumor angiography with an oxygen tension heat map to the left and bottom of the angiography image. The depths of the heat maps go from 50 μm to 200 μm and are taken from the planes noted by the white lines in the angiography image. In the angiography, color denotes depth (from deep to shallow: green, red, white). The color scale of the oxygen heat maps is shown in the bottom panel (blue indicates 0 mm Hg oxygen tension, whereas red indicates 45 mm Hg). Black outlines on the oxygen heat maps indicate the morphometry of the tumor vessels. Scale bar, 500 μm in all panels. **B,** Oxygen tension maps from 50 μm, 100 μm, 150 μm, and 200 μm deep within the tumor are shown in **A**. The angiographic depth slice at 50 μm is shown above the 50 μm deep oxygen heat map for comparison. Black lines on the oxygen heat maps indicate the morphometry of the tumor vessels. **C,** Angiography of an MCaIV tumor. Asterisk (*) indicates an area lacking perfused vessels. Color denotes depth (from deep to shallow: green, red, white). **D,** Scatter plot of extravascular (interstitial, i.e., measurements 40 to 60 μm from the nearest vessel) oxygen tension (mm Hg) versus the diameter of the nearest vessel (μm) in MCaIV tumors. Data pooled from four mice. **E,** Angiography of an E0771 tumor. **F,** Scatter plot of extravascular (interstitial, i.e., measurements 40–60 μm from the nearest vessel) oxygen tension versus the diameter of the nearest vessel in E0771 tumors. Data pooled from five mice. **G,** Measurements of oxygen tension in mm Hg in blood vessels in skin and tumor models. Lines indicate statistically significant differences between multiple comparisons after a Kruskal–Wallis test with Dunn's correction. **H,** Measurements of extravascular oxygen tension in mm Hg normalized to the intravascular oxygen tension of blood vessels in skin and tumor tissues.

Downloaded from http://aacrjournals.org/clincancerres/article-pdf/28/14/3076/3186259/3076.pdf by guest on 21 September 2023

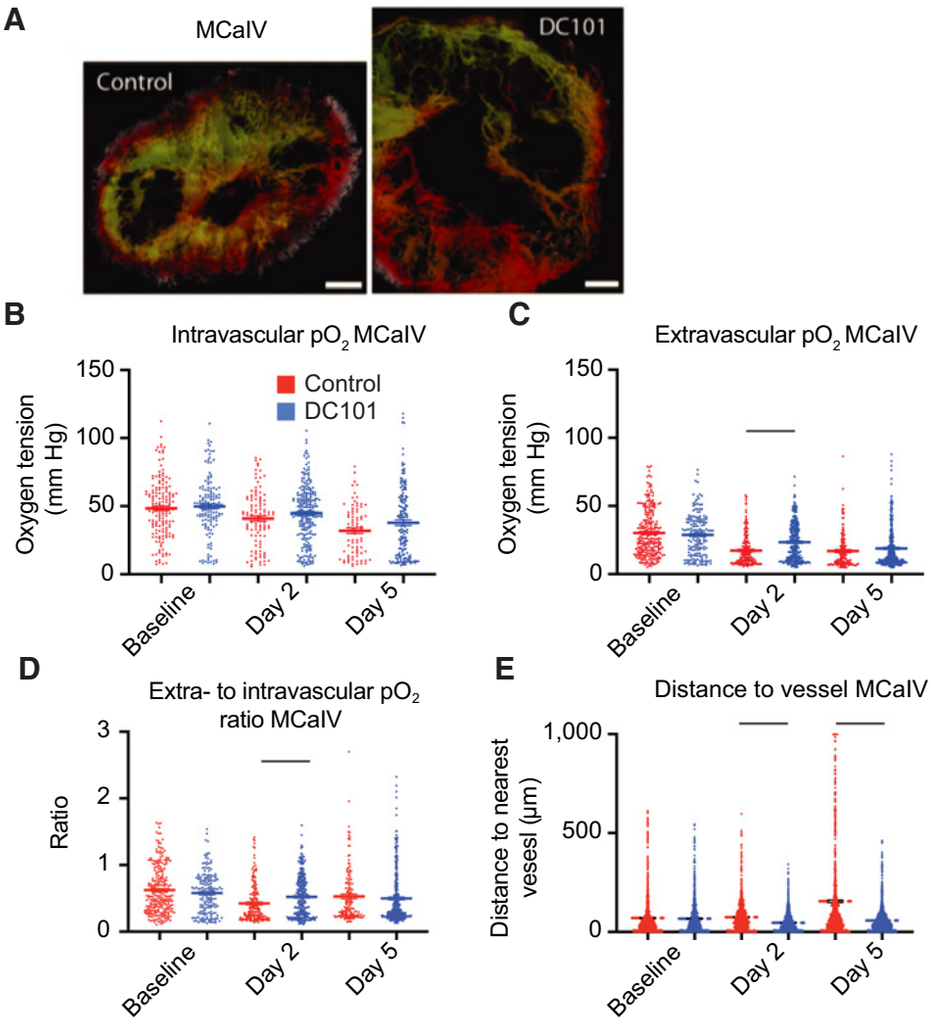

Figure 4.
Anti-VEGFR2 antibody treatment at 40 mg/kg transiently increases interstitial pO_2 on day 2 and restores perfusion in MCaIV. **A,** Representative images of angiography of murine mammary carcinoma (MCaIV) tumors treated with control IgG (left) and murine anti-VEGFR2 antibody DC101 (right; both 40 mg/kg i.p. every 3 days) on day 5 after two cycles of treatment. Tumor vasculature is presented as a colorized maximum intensity depth projection (superficial to deep: green, red, white). Scale bars, 500 µm. **B,** Measurements of oxygen tension in mm Hg in vessels in control IgG and DC101 antibody-treated mice at baseline, day 2, and day 5. n = 81–226 measurements per time point per group. N = 4 mice per group. Horizontal black lines indicate statistically significant differences between multiple comparisons after a Kruskal–Wallis test with Dunn's correction, with differences only depicted for comparisons between control and treatment groups on the same day. **C,** Extravascular (interstitial, i.e., measurements 40–60 µm from the nearest vessel) oxygen measurements in the same tumors. n = 138–328 measurements per time point per group. **D,** Measurements of extravascular oxygen tension in mm Hg normalized to the intravascular oxygen tension of blood vessels. **E,** Distance to the nearest vessel measurements in the same tumors. n = 1,117–1,851 measurements per group.

nanoparticles (33) or homogeneous distribution of perfused vessels (12). As with MCaIV, oxygenation in control IgG-treated E0771 tumors decreased with tumor growth (**Fig. 5B** and **C**). Unlike MCaIV, neither intravascular nor extravascular oxygenation in 40 mg/kg DC101-treated tumors was different compared with controls on day 2 (**Fig. 5B** and **C**). The intravascular oxygen tension on day 2 was only 50% of that of vessels in the skin in IgG-treated E0771 tumor vessels, and 67% of that in skin vessels in DC101-treated tumor vessels.

In addition to negligible effects on oxygen tension, the 40 mg/kg dose of DC101 also caused detrimental effects on the distribution of perfused vessels in E0771 tumors as shown by larger avascular regions (**Fig. 5A**). DC101 increased the mean and maximum distance to the nearest vessel on day 5 by 91% and 210%, respectively, compared with these distances in IgG-treated tumors (**Fig. 5D**). DC101 treatment pruned vessels as indicated by reduced total perfused microvascular density (MVD; Supplementary Fig. S10), which is consistent with the larger distances to the nearest vessel in the 40 mg/kg group. To understand which subpopulation of vessels was pruned, we examined how DC101 changes the distribution of vessel diameters between baseline and day 5 by plotting the frequencies of diameters in a histogram and found that there are fewer vessels less than 20 µm in diameter and more vessels greater than 20 µm in diameter on day 5 (Supplementary Fig. S11) compared with control (Supplementary Fig. S12). Indeed, the fraction of vessels less than 20 µm in diameter on day 5 was 25% in DC101-treated E0771 tumors compared with 44% in control. This small vessel pruning effect matched that of bevacizumab in breast cancer patients, as small vessels were selectively pruned in a representative patient (Supplementary Fig. S13; ref. 20). Thus, a 40 mg/kg dose of DC101 prunes small vessels resulting in large avascular regions in E0771 tumors.

To gain insight into the effect of DC101 on vessel function, we correlated the size of the nearest vessel to interstitial oxygenation (i.e., measurements 40–60 µm from the nearest vessel) on day 5 (**Fig. 5E** and **F**). In normal tissues, the diameter of a vessel is positively correlated to the flow rate (34) and thus the amount of oxygen delivered (**Fig. 2E**). Surprisingly, in DC101-treated E0771 tumors, smaller tumor vessels were associated with greater extravascular oxygen than larger tumor vessels as indicated by a statistically significant negative correlation coefficient (**Fig. 5F**). Thus, the small vessels remaining after pruning deliver oxygen efficiently compared with the large vessels.

Interestingly, DC101-treated tumors had lower vessel efficiency than control tumors on days 2 and 5 (**Fig. 5G**). The reduced vessel

Downloaded from http://aacrjournals.org/clincancerres/article-pdf/28/14/3076/3186259/3076.pdf by guest on 21 September 2023

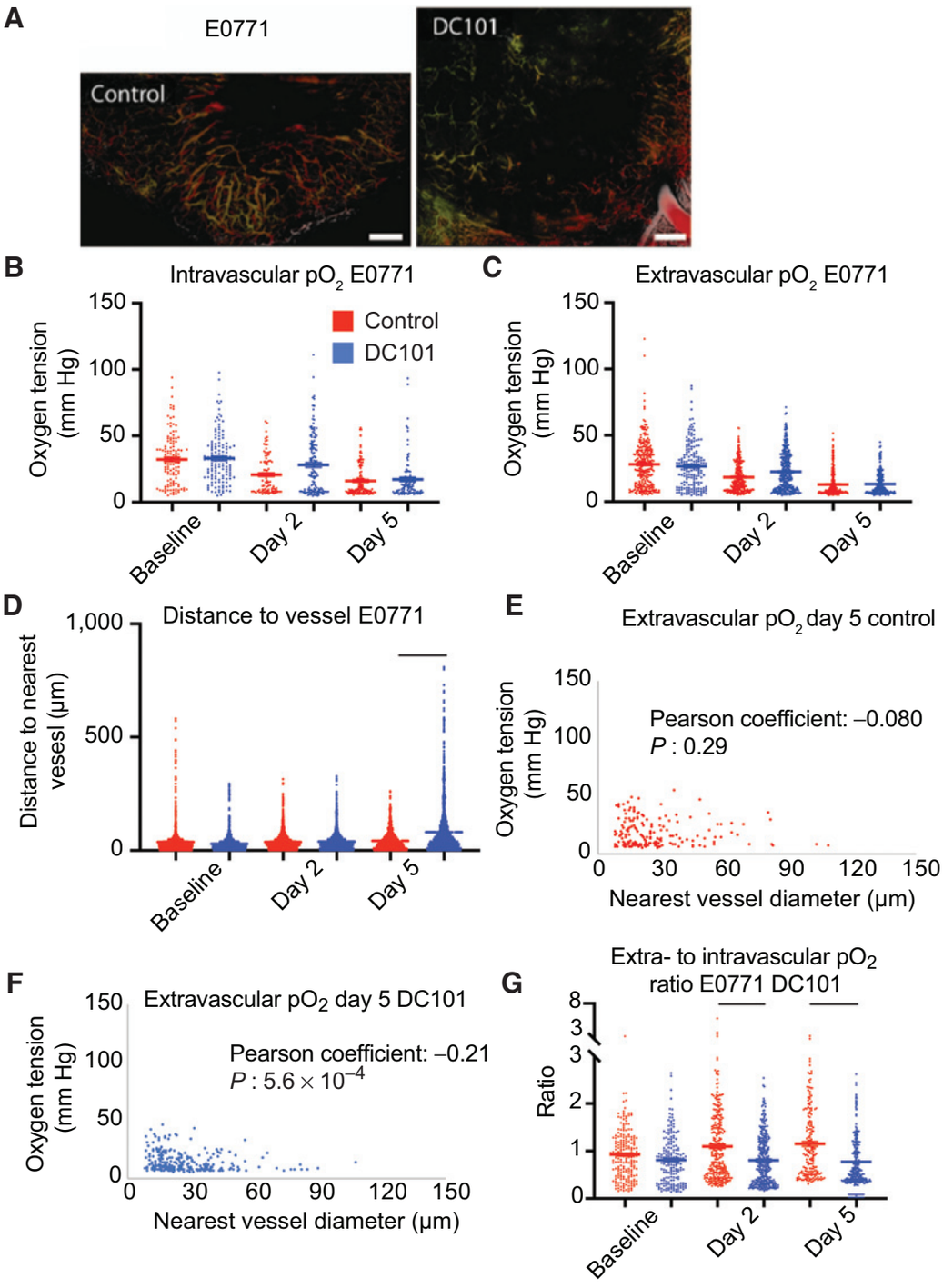

Figure 5.

Anti-VEGFR2 antibody treatment at 40 mg/kg does not affect pO_2 but extensively prunes the smallest microvessels by day 5 in E0771. **A,** Representative images of angiographies of murine mammary carcinoma (E0771) tumors treated with control IgG antibody (left) or the murine anti-VEGFR2 antibody DC101 (right; both 40 mg/kg i.p. every 3 days) on day 5 after two cycles of treatment. Tumor vasculature is presented as a colorized maximum intensity depth projection (superficial to deep: green, red, white). Scale bars, 500 µm. **B,** Measurements of oxygen tension in mm Hg in vessels in control IgG and 40 mg/kg DC101 antibody-treated mice at baseline, day 2, and day 5. $n = 92–139$ measurements per time point per group. $N = 5$ mice per group. Lines indicate statistically significant differences between multiple comparisons after a Kruskal–Wallis test with Dunn's correction, with differences only depicted for comparisons between control and treatment groups on the same day. **C,** Extravascular (interstitial, i.e., measurements 40–60 µm from the nearest vessel) oxygen measurements in the same tumors. $n = 179–307$ measurements per time point per group. **D,** Distance to the nearest vessel measurements in the same tumors. $n = 1{,}103–1{,}961$ measurements per time point per group. **E,** Scatter plot of extravascular oxygen tension versus the diameter of the nearest vessel in control-treated E0771 tumors on day 5. Correlation coefficient and *P* value are denoted on the graph. **F,** Scatter plot of extravascular oxygen tension versus the diameter of the nearest vessel in DC101-treated E0771 tumors on day 5. Correlation coefficient and *P* value are denoted on the graph. **G,** Measurements of extravascular oxygen tension in mm Hg normalized to the intravascular oxygen tension of blood vessels.

Downloaded from http://aacrjournals.org/clincancerres/article-pdf/28/14/3076/3186259/3076.pdf by guest on 21 September 2023

efficiency we observed could be a result of enhanced consumption of oxygen or the large distance between perfused vessels reducing the contribution to extravascular oxygen by nearby vessels. Thus, DC101 induced negligible effects on intravascular and extravascular oxygenation in desmoplastic E0771 breast tumors, and through pruning of small and inefficient vessels, eventually resulted in an insufficient network of perfused vessels.

A lower dose of AAT enhances individual vessel function without excessive vessel pruning in E0771

As DC101 resulted in excessive vessel pruning in E0771 tumors, we investigated the response to lower-dose DC101, previously shown to normalize vessel function (nanoparticle extravasation and reduced heterogeneity) in murine models of breast cancer (12, 33). However, it remained unknown to what extent lower doses of AAT, which may not cause pruning, can enhance individual vessel function. Using an eighth of the dose of DC101 (5 mg/kg; ref. 33) to treat E0771 tumors, we measured increased intravascular (**Fig. 6A**) and extravascular (**Fig. 6B**) oxygenation on day 2 compared with IgG treatment. There was no difference in lower-dose DC101 and IgG treatment on day 5. Multiple linear regression analysis revealed that intravascular oxygenation in the control group decreased between days 0 and 2 at a rate of 2.8 mm Hg/day ($P = 0.048$ compared with no change over time), and it increased in the lower-dose DC101 group at a rate of 3.7 mm Hg/day ($P = 0.0012$ compared with the control group's rate; Supplementary Table S4). Extravascular oxygenation in the control group decreased between days 0 and 2 at a rate of 4.4 mm Hg/day ($P < 0.0001$ compared with no change over time), and it increased in the DC101 group at a rate of 1.5 mm Hg/day ($P < 0.0001$ compared with the control group's rate; Supplementary Table S5). The intravascular oxygen tension in IgG-treated E0771 tumors on day 2 was 71% of that of vessels in skin, whereas the oxygen tension reached 98% in 5 mg/kg DC101-treated tumor vessels. Compared with the 40 mg/kg dose DC101, 5 mg/kg treatment in E0771 postponed the onset of lesser vessel efficiency compared with controls, which was affected by the low intravascular oxygenation of control tumor blood vessels, from days 2 to 5 (**Fig. 6C**).

We next investigated the effect of lower-dose DC101 on vessel pruning. Unlike the 40 mg/kg dose, the 5 mg/kg dose DC101 decreased the average and maximum distance to a vessel on day 5 by 36% and 48%, respectively, compared with control (**Fig. 6D**). Thus, 5 mg/kg DC101 induces superior transient normalization of individual vessels. By avoiding the detrimental pruning observed after higher dose treatment, lower dose treatment restored perfusion to hypoperfused regions.

Angiotensin system inhibition increases extravascular oxygenation after reperfusing small, nonfunctional vessels in E0771

Experimental and theoretical studies indicate that reversing vessel compression—by reducing the compressive force generated by the growing tumor—using cancer-associated fibroblast reprogramming agents, such as the ARB losartan, can enhance oxygen delivery to desmoplastic tumors by converting nonfunctional vessels to perfused vessels (5, 25, 26). However, the effects of cancer-associated fibroblast reprogramming through angiotensin system inhibition on oxygen delivery from individual vessels are not known. Thus, we investigated how losartan affects oxygenation and the distribution of perfused vessels in E0771 breast tumors. Although losartan did not affect intravascular oxygenation (**Fig. 6E**), it led to 61% greater extravascular oxygenation compared with controls on day 5 after treatment initiation (**Fig. 6F**). Multiple linear regression analysis revealed that extravascular oxygenation in the control group decreased between days 2 and 5 at a rate of 1.9 mm Hg/day ($P = 0.0049$ compared with no change over time), and it increased in the losartan group at a rate of 2.0 mm Hg/day ($P = 0.0002$ compared with the control group's rate; Supplementary Table S6).

The perfused vessels in losartan-treated tumors were closer to each other by day 2, as there were shorter mean distances to the nearest vessels (**Fig. 6G**). On days 2 and 5, the mean distance was 19% and 38% less than controls, respectively. Because losartan may decompress vessels without affecting vessel fortification (5), we next investigated the correlation between nearest vessel diameter and interstitial oxygenation at the individual vessel level (**Fig. 6H** and **I**). Losartan-treated tumors exhibited a positive correlation between extravascular oxygen tension and the diameter of the nearest vessel (**Fig. 6I**) similar to normal tissues, with larger vessels supplying more oxygen. Losartan increased perfused MVD (5), and plotting the frequencies of vessel diameters in a histogram revealed that by day 5, losartan increased the number of vessels with diameters between 12 and 30 μm and maintained the number of small vessels less than 12 μm (Supplementary Fig. S14). The latter are the vessel type pruned by DC101 (Supplementary Fig. S11). The greater extravascular oxygenation on day 5 was likely caused by the reperfused vessels, as vascular efficiency was unaffected with losartan treatment (**Fig. 6J**). Thus, losartan decreases the size of avascular regions by day 2, which leads to greater extravascular oxygenation relative to control tumors by day 5.

Discussion

We report here a new approach to dynamically evaluate the effects of treatment on the function and distribution of blood vessels. Capillaries in normal tissues supply more oxygen as they are densely and evenly distributed in tissues. This pattern is lost in most tumors, as there are spatial and temporal heterogeneities within a tumor, between lesions in the same patient and across patients with the same cancer type (2). Indeed, we observed different responses in two murine breast cancer models that represent different subtypes of breast cancer. In MCaIV, a 40 mg/kg dose of DC101 transiently increased extravascular oxygen delivery by day 2 and restored perfusion, whereas in E0771, 40 mg/kg DC101 did not affect oxygen delivery despite pruning vessels. In contrast, a lower dose of DC101 treatment of E0771 tumors increased intravascular and extravascular oxygen delivery on day 2 and restored perfusion on day 5. These results are consistent with various clinical studies highlighting the importance of AAT dose and disparate responses of patients with the same tumor type (1, 2, 15).

Although AAT is known to prune immature vessels in mice after a couple of days, AAT improves single-vessel function within 6 hours (11) and alleviates hypoxia within two days by inducing pericyte recruitment via Ang1/Tie2 signaling (9). In the E0771 breast tumor model, 40 mg/kg AAT reduced the number of small vessels without affecting larger functional vessels on day 5. One potential strategy to avoid too much vessel pruning—resulting in increased hypoperfusion—would be to induce vessel fortification by nonpruning AAT (47).

We also found that losartan enhances oxygen delivery by maintaining the density of small diameter vessels in desmoplastic E0771 breast tumors, which reduces over time in untreated controls. These data provide additional mechanistic insights into multiple retrospective studies, indicating that drugs like losartan correlate with longer survival in cancer patients (26, 48–50). The kinetics of functional vessel remodeling with losartan differ from AAT. In the tumor models we examined, losartan reperfuses small, poorly functioning vessels by

Downloaded from http://aacrjournals.org/clincancerres/article-pdf/28/14/3076/3186259/3076.pdf by guest on 21 September 2023

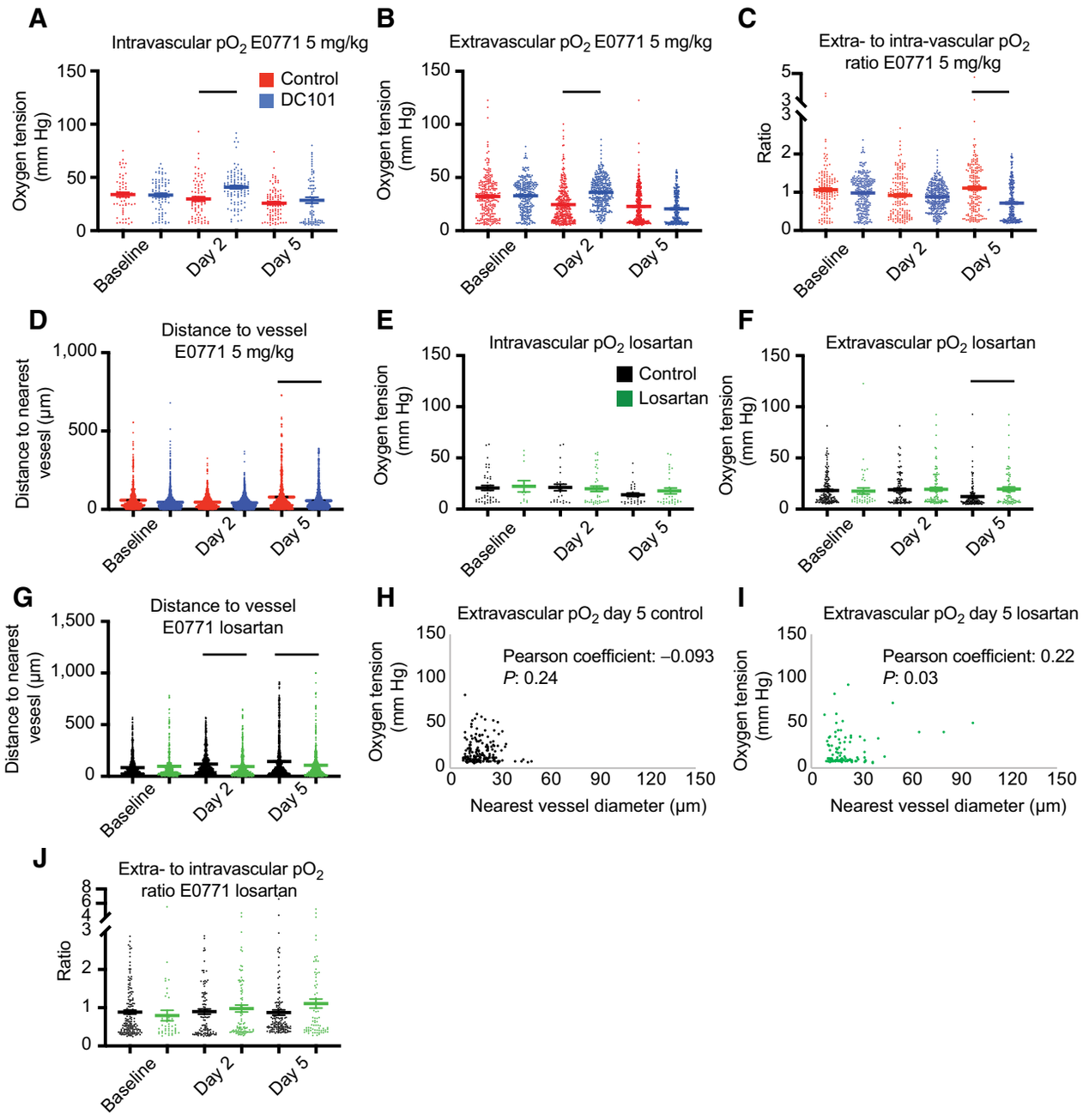

Figure 6.

Anti-VEGFR2 antibody treatment at 5 mg/kg increases intravascular and interstitial pO_2 while restoring perfusion (**A–D**), whereas losartan increases interstitial pO_2 on day 5 after reperfusing vessels on day 2 in E0771 (**E–J**). **A,** Measurements of intravascular oxygen tension in mm Hg in control IgG and anti-VEGFR2 (DC101) (both 5 mg/kg i.p. every 3 days) antibody-treated mice at baseline, day 2, and day 5. $n = 64–103$ measurements per time point per group. $N = 5–8$ mice per group in the DC101 studies. Lines indicate statistically significant differences between multiple comparisons after a Kruskal–Wallis test with Dunn's correction, with differences depicted only for comparisons between control and treatment groups on the same day. **B,** Extravascular (interstitial, i.e., measurements 40–60 µm from the nearest vessel) oxygen measurements in the same tumors. $n = 246–367$ measurements per time point per group. **C,** Measurements of extravascular oxygen tension in mm Hg normalized to the intravascular oxygen tension of blood vessels. **D,** Distance to the nearest vessel measurements in the same tumors. $n = 870–1,962$ measurements per time point per group. **E,** Measurements of intravascular oxygen tension in mm Hg in control PBS and losartan-treated mice at baseline, day 2, and day 5. $n = 12–38$ measurements per time point per group. $N = 4–6$ mice per group. **F,** Extravascular (interstitial, i.e., measurements 40–60 µm from the nearest vessel) oxygen measurements in the same tumors. $n = 42–161$ measurements per time point per group. $N = 4–6$ mice per group. **G,** Distance to the nearest vessel measurements in the same tumors. $n = 412–1,279$ measurements per time point per group. **H,** Scatter plot of interstitial oxygen tension versus the diameter of the nearest vessel in E0771 control-treated tumors on day 5. Correlation coefficient and *P* value are denoted on the graph. **I,** Scatter plot of interstitial oxygen tension versus the diameter of the nearest vessel in E0771 losartan-treated tumors on day 5. Correlation coefficient and *P* value are denoted on the graph. **J,** Measurements of extravascular oxygen tension in mm Hg normalized to the intravascular oxygen tension of blood vessels.

Downloaded from http://aacrjournals.org/clincancerres/article-pdf/28/14/3076/3186259/3076.pdf by guest on 21 September 2023

day 2—consistent with data from glioblastoma patients (51)—whereas AAT can cause pruning of similar vessels in patients with lower baseline tumor VEGF. In our phase II trial in GBM patients, we observed an increased blood flow rate in some patients and decreased blood flow in others in response to the identical dose and schedule of VEGF inhibition (16). Our hypothesis is that these differential changes in the blood flow rate were dependent on the baseline levels of VEGF in these tumors. However, better outcomes in patients were consistently correlated with the extent of functional normalization (13–16, 20).

Losartan also improves the oxygen delivery function of individual vessels compared with control later than AAT (i.e., on day 5 vs. transiently on day 2) in mice. The normalization window can last more than a month in humans (14, 16). The finding that losartan improves extravascular oxygen tension compared with control on day 5 suggests that decompression allows blood to flow in more vessels, thereby providing more vessels to supply extravascular oxygen to tissue. These results likely are dependent on the tumor model. The mechanisms associated with the rapid increase of perfused vessel density followed by greater single-vessel function need to be investigated in future studies.

Our data indicate small, reperfused vessels after losartan treatment are less efficient in delivering oxygen to the interstitial space than the larger microvessels, even though they have a positive effect on increasing tissue oxygen compared with no vessel perfusion. These findings support the notion that vessels newly reperfused by agents like losartan are immature functionally. Our hypothesis that losartan treatment should be combined with normalizing doses of AAT to fortify newly reperfused, immature vessels needs to be tested in independent studies. Of note, in moderately desmoplastic breast tumor types, our mathematical model predicts enhanced vascular function by combining AAT and decompressing agents (21, 52), whereas experimental studies have demonstrated that agents that simultaneously act as AAT and decompressing agents increase vessel function (53, 54). Importantly, vessel decompressing agents, including losartan, often have pleiotropic effects including directly and indirectly affecting immune cells (49). The latter may also contribute to vascular normalization resulting in increased perfusion and efficacy of immune-checkpoint blockers (55).

The system of MP-PQM we developed is subject to several limitations. The maximum oxygen detectable is 122 mm Hg. However, we rarely encountered measurements approaching this value in tumors, and this technique is more accurate at lower oxygen tensions because of the longer quenching time. The maximum tissue depth that can be imaged is 300 μm, but the tumors we imaged had diameters at least 3.0 mm. Thus, the tumor center cannot be entirely probed. Fluorescence imaging and PQM are performed serially rather than in parallel, thereby increasing the experiment time.

Our study provided new insights into the kinetics of increased vascular function with AAT and losartan at single-vessel resolution. Depending on the tumor model and dose, AAT enhances vascular function compared with control on day 2 and restores perfusion or does not affect vascular function. In the latter "unresponsive" model (i.e., E0771), a lower dose of AAT enhanced vascular function and improved perfusion. In the same "unresponsive" model, losartan enhances vascular function compared with control on day 5 and had greater perfused vessel density compared with control on day 2. AAT prunes poorly functioning small vessels, whereas vessels reperfused with losartan are small, poorly functioning vessels. Thus, combining these two tumor microenvironmental normalizing strategies has the potential to enhance treatment further (21, 52). In fact, a recent retrospective analysis showed survival benefits in patients who received a combination of anti-VEGF agents and angiotensin system inhibitors with immune-checkpoint blockers (50). Thus, future work is needed to identify the optimal dose and sequence of these two normalization strategies.

Authors' Disclosures

J.D. Martin reports personal fees from Nanocarrier Co., Ltd. outside the submitted work. R.M. Lanning reports grants from the Department of Defense Breast Cancer Research Program during the conduct of the study. V.P. Chauhan reports a patent for 13/834,094 pending and a patent for 16/063,353 pending. A.S. Mousa reports other support from Pieris Pharmaceuticals, Inc. outside the submitted work. W.S. Kamoun reports personal fees from Servier outside the submitted work. D.G. Duda reports personal fees from Innocoll and grants from BMS, Bayer, Exelixis, and Surface Oncology outside the submitted work. T.P. Padera reports grants from NIH during the conduct of the study, and personal fees from PureTech Health outside the submitted work. R.K. Jain reports grants from Jane's Trust Foundation, the Nile Albright Research Foundation, the National Foundation for Cancer Research, The Ludwig Center at Harvard Medical School, and the US NCI during the conduct of the study; personal fees from Elpis, Innocoll, and SPARC, personal fees and other support from SynDevRx, and other support from Accurius, Enlight, Tekla Healthcare Investors, Tekla Life Sciences Investors, Tekla Healthcare Opportunities Fund, and Tekla World Healthcare Fund outside the submitted work; and states that no regents or funding from any of these companies was used to support this research. No disclosures were reported by the other authors.

Authors' Contributions

J.D. Martin: Conceptualization, data curation, software, formal analysis, investigation, visualization, methodology, writing–original draft, writing–review and editing. **R.M. Lanning:** Conceptualization, data curation, software, formal analysis, validation, investigation, visualization, methodology, writing–original draft, writing–review and editing. **V.P. Chauhan:** Conceptualization, formal analysis, investigation, methodology, writing–review and editing. **M.R. Martin:** Formal analysis, writing–review and editing. **A.S. Mousa:** Investigation, writing–review and editing. **W.S. Kamoun:** Conceptualization, data curation, software, formal analysis, validation, investigation, visualization, methodology. **H.-S. Han:** Investigation, writing–review and editing. **H. Lee:** Methodology, writing–review and editing. **T. Stylianopoulos:** Methodology, writing–review and editing. **M.G. Bawendi:** Supervision, funding acquisition, writing–review and editing. **D.G. Duda:** Supervision, writing–original draft, writing–review and editing. **E.B. Brown:** Supervision, methodology, writing–review and editing. **T.P. Padera:** Methodology, writing–original draft, writing–review and editing. **D. Fukumura:** Conceptualization, supervision, funding acquisition, writing–original draft, project administration, writing–review and editing. **R.K. Jain:** Conceptualization, supervision, funding acquisition, writing–original draft, project administration, writing–review and editing.

Acknowledgments

The authors thank Julia Kahn, Sylvie Roberge, and Elisabeth Niemeyer for their technical assistance. R.K. Jain's research is supported by grants from the Jane's Trust Foundation, the Nile Albright Research Foundation, the National Foundation for Cancer Research, the Ludwig Center at Harvard Medical School, the US NCI grants R35CA197743, R01CA259253, R01269672, U01CA261842, and U01CA224348. R.K. Jain's and D. Fukumura's research is supported by NCI grant R01-CA208205. D. Fukumura's work is also supported by NIH grant R01NS118929. D.G. Duda's work is supported by NIH grants R01CA260872, R01CA260857, R01CA247441, and R03CA256764, and by Department of Defense grants W81XWH-19-1-0284 and W81XWH-21-1-0738. T.P. Padera's research is supported by US National Institute of Health grants R01CA214913, R01HL128168, R21AI135092, and R21AG072205 and by the Rullo Family MGH Research Scholar Award.

The costs of publication of this article were defrayed in part by the payment of page charges. This article must therefore be hereby marked *advertisement* in accordance with 18 U.S.C. Section 1734 solely to indicate this fact.

Received February 13, 2022; revised April 14, 2022; accepted May 11, 2022; published first June 23, 2022.

Downloaded from http://aacrjournals.org/clincancerres/article-pdf/28/14/3076/3186259/3076.pdf by guest on 21 September 2023

References

1. Jain RK. Antiangiogenesis strategies revisited: from starving tumors to alleviating hypoxia. Cancer Cell 2014;26:605–22.
2. Martin JD, Seano G, Jain RK. Normalizing function of tumor vessels: progress, opportunities and challenges. Annu Rev Physiol 2019;81:505–34.
3. Jain RK, Martin JD, Stylianopoulos T. The role of mechanical forces in tumor growth and therapy. Annu Rev Biomed Eng 2014;16:321–46.
4. Nia HT, Munn LL, Jain RK. Physical traits of cancer. Science 2020;370:eaaz0868.
5. Chauhan VP, Martin JD, Liu H, Lacorre DA, Jain SR, Kozin SV, et al. Angiotensin inhibition enhances drug delivery and potentiates chemotherapy by decompressing tumour blood vessels. Nat Commun 2013;4:2516.
6. Baish JW, Stylianopoulos T, Lanning RM, Kamoun WS, Fukumura D, Munn LL, et al. Scaling rules for diffusive drug delivery in tumor and normal tissues. Proc Natl Acad Sci U S A 2011;108:1799–803.
7. Jain RK. Normalizing tumor vasculature with anti-angiogenic therapy: a new paradigm for combination therapy. Nat Med 2001;7:987–9.
8. Jain RK. Normalization of tumor vasculature: an emerging concept in anti-angiogenic therapy. Science 2005;307:58–62.
9. Winkler F, Kozin SV, Tong RT, Chae S-S, Booth MF, Garkavtsev I, et al. Kinetics of vascular normalization by VEGFR2 blockade governs brain tumor response to radiation: role of oxygenation, angiopoietin-1, and matrix metalloproteinases. Cancer Cell 2004;6:553–63.
10. Tong RT, Boucher Y, Kozin SV, Winkler F, Hicklin DJ, Jain RK. Vascular normalization by vascular endothelial growth factor receptor 2 blockade induces a pressure gradient across the vasculature and improves drug penetration in tumors. Cancer Res 2004;64:3731–6.
11. Yuan F, Chen Y, Dellian M, Safabakhsh N, Ferrara N, Jain RK. Time-dependent vascular regression and permeability changes in established human tumor xenografts induced by an anti-vascular endothelial growth factor/vascular permeability factor antibody. Proc Natl Acad Sci U S A 1996;93:14765–70.
12. Huang Y, Yuan J, Righi E, Kamoun WS, Ancukiewicz M, Nezivar J, et al. Vascular normalizing doses of antiangiogenic treatment reprogram the immunosuppressive tumor microenvironment and enhance immunotherapy. Proc Natl Acad Sci U S A 2012;109:17561–6.
13. Heist RS, Duda DG, Sahani DV, Ancukiewicz M, Fidias P, Sequist LV, et al. Improved tumor vascularization after anti-VEGF therapy with carboplatin and nab-paclitaxel associates with survival in lung cancer. Proc Natl Acad Sci U S A 2015;112:1547–52.
14. Sorensen AG, Emblem KE, Polaskova P, Jennings D, Kim H, Ancukiewicz M, et al. Increased survival of glioblastoma patients who respond to antiangiogenic therapy with elevated blood perfusion. Cancer Res 2012;72:402–7.
15. Gerstner ER, Emblem KE, Chang K, Vakulenko-Lagun B, Yen Y-F, Beers AL, et al. Bevacizumab reduces permeability and concurrent temozolomide delivery in a subset of patients with recurrent glioblastoma. Clin Cancer Res 2019;26:206–12.
16. Batchelor TT, Gerstner ER, Emblem KE, Duda DG, Kalpathy-Cramer J, Snuderl M, et al. Improved tumor oxygenation and survival in glioblastoma patients who show increased blood perfusion after cediranib and chemoradiation. Proc Natl Acad Sci U S A 2013;110:19059–64.
17. Boucher Y, Kumar AS, Posada JM, Gjini E, Pfaff K, Lipschitz M, et al. Bevacizumab improves tumor infiltration of mature dendritic cells and effector T-cells in triple-negative breast cancer patients. NPJ Precis Oncol 2021;5:62.
18. Jain RK. Normalizing tumor microenvironment to treat cancer: bench to bedside to biomarkers. J Clin Oncol 2013;31:2205–18.
19. Vakoc BJ, Lanning RM, Tyrrell JA, Padera TP, Bartlett LA, Stylianopoulos T, et al. Three-dimensional microscopy of the tumor microenvironment in vivo using optical frequency domain imaging. Nat Med 2009;15:1219–23.
20. Tolaney SM, Boucher Y, Duda DG, Martin JD, Seano G, Ancukiewicz M, et al. Role of vascular density and normalization in response to neoadjuvant bevacizumab and chemotherapy in breast cancer patients. Proc Natl Acad Sci U S A 2015;112:14325–30.
21. Stylianopoulos T, Jain RK. Combining two strategies to improve perfusion and drug delivery in solid tumors. Proc Natl Acad Sci U S A 2013;110:18632–7.
22. Griffon-Etienne G, Boucher Y, Brekken C, Suit HD, Jain RK. Taxane-induced apoptosis decompresses blood vessels and lowers interstitial fluid pressure in solid tumors: clinical implications. Cancer Res 1999;59:3776–82.
23. Padera TP, Stoll BR, Tooredman JB, Capen D, Tomaso ED, Jain RK. Pathology: cancer cells compress intratumour vessels. Nature 2004;427:695.
24. Diop-Frimpong B, Chauhan VP, Krane S, Boucher Y, Jain RK. Losartan inhibits collagen I synthesis and improves the distribution and efficacy of nanotherapeutics in tumors. Proc Natl Acad Sci U S A 2011;108:2909–14.
25. Chauhan VP, Chen IX, Tong R, Ng MR, Martin JD, Naxerova K, et al. Reprogramming the microenvironment with tumor-selective angiotensin blockers enhances cancer immunotherapy. Proc Natl Acad Sci U S A 2019;116:10674–80.
26. Zhao Y, Cao J, Melamed A, Worley M, Gockley A, Jones D, et al. Losartan treatment enhances chemotherapy efficacy and reduces ascites in ovarian cancer models by normalizing the tumor stroma. Proc Natl Acad Sci U S A 2019;116:2210–9.
27. Brown EB, Campbell RB, Tsuzuki Y, Xu L, Carmeliet P, Fukumura D, et al. In vivo measurement of gene expression, angiogenesis and physiological function in tumors using multiphoton laser scanning microscopy. Nat Med 2001;7:864–8.
28. Torres Filho IP, Leunig M, Yuan F, Intaglietta M, Jain RK. Noninvasive measurement of microvascular and interstitial oxygen profiles in a human tumor in SCID mice. Proc Natl Acad Sci U S A 1994;91:2081–5.
29. Helmlinger G, Yuan F, Dellian M, Jain RK. Interstitial pH and pO2 gradients in solid tumors in vivo: high-resolution measurements reveal a lack of correlation. Nat Med 1997;3:177–82.
30. Sakadžić S, Roussakis E, Yaseen MA, Mandeville ET, Srinivasan VJ, Arai K, et al. Two-photon high-resolution measurement of partial pressure of oxygen in cerebral vasculature and tissue. Nat Methods 2010;7:755–9.
31. Spencer JA, Ferraro F, Roussakis E, Klein A, Wu J, Runnels JM, et al. Direct measurement of local oxygen concentration in the bone marrow of live animals. Nature 2014;508:269–73.
32. Han H-S, Niemeyer E, Huang Y, Kamoun WS, Martin JD, Bhaumik J, et al. Quantum dot/antibody conjugates for in vivo cytometric imaging in mice. Proc Natl Acad Sci U S A 2015;112:1350–5.
33. Chauhan VP, Stylianopoulos T, Martin JD, Popović Z, Chen O, Kamoun WS, et al. Normalization of tumour blood vessels improves the delivery of nanomedicines in a size-dependent manner. Nat Nanotechnol 2012;7:383–8.
34. Yuan F, Salehi HA, Boucher Y, Vasthare US, Tuma RF, Jain RK. Vascular permeability and microcirculation of gliomas and mammary carcinomas transplanted in rat and mouse cranial windows. Cancer Res 1994;54:4564–8.
35. Matsuda Y, Ohsaka K, Yamamoto H, Natsume K, Hirabayashi S, Kounoike M, et al. Comparison of newly developed inhalation anesthesia system and intraperitoneal anesthesia on the hemodynamic state in mice. Biol Pharm Bull 2007;30:1716–20.
36. Ziemer LS, Lee WMF, Vinogradov SA, Sehgal C, Wilson DF. Oxygen distribution in murine tumors: characterization using oxygen-dependent quenching of phosphorescence. J Appl Physiol 2005;98:1503–10.
37. Wen B, Urano M, O'Donoghue JA, Ling CC. Measurements of partial oxygen pressure using the OxyLite system in R3327-AT tumors under isoflurane anesthesia. Radiat Res 2006;166:512–8.
38. McGraw CM, Khalil G, Callis JB. Comparison of time and frequency domain methods for luminescence lifetime measurements. J Phys Chem C 2008;112:8079–84.
39. O'Donovan C, Hynes J, Yashunski D, Papkovsky DB. Phosphorescent oxygen-sensitive materials for biological applications. J Mater Chem 2005;15:2946–51.
40. Kruk M, Karotki A, Drobizhev M, Kuzmitsky V, Gael V, Rebane A. Two-photon absorption of tetraphenylporphin free base. J Lumin 2003;105:45–55.
41. Lakowicz J. Principles of fluorescence microscopy. New York: Kluwer Academic, 1999.
42. Jain RK. Determinants of tumor blood flow: a review. Cancer Res 1988;48:2641–58.
43. Ricard C, Stanchi F, Rodriguez T, Amoureux M-C, Rougon G, Debarbieux F. Dynamic quantitative intravital imaging of glioblastoma progression reveals a lack of correlation between tumor growth and blood vessel density. PLoS One 2013;8:e72655.
44. Han H-S, Martin JD, Lee J, Harris DK, Fukumura D, Jain RK, et al. Spatial charge configuration regulates nanoparticle transport and binding behavior in vivo. Angew Chem Int Ed 2013;52:1414–9.
45. Hashizume H, Baluk P, Morikawa S, McLean JW, Thurston G, Roberge S, et al. Openings between defective endothelial cells explain tumor vessel leakiness. Am J Pathol 2000;156:1363–80.
46. Panagi M, Voutouri C, Mpekris F, Papageorgis P, Martin MR, Martin JD, et al. TGF-β inhibition combined with cytotoxic nanomedicine normalizes triple negative breast cancer microenvironment towards anti-tumor immunity. Theranostics 2020;10:1910–22.

Downloaded from http://aacrjournals.org/clincancerres/article-pdf/28/14/3076/3186259/3076.pdf by guest on 21 September 2023

47. Goel S, Gupta N, Walcott BP, Snuderl M, Kesler CT, Kirkpatrick ND, et al. Effects of vascular-endothelial protein tyrosine phosphatase inhibition on breast cancer vasculature and metastatic progression. J Natl Cancer Inst 2013;105:1188–201.
48. Martin JD, Cabral H, Stylianopoulos T, Jain RK. Improving cancer immunotherapy using nanomedicine: progress, opportunities and challenges. Nat Rev Clin Oncol 2020;17:251–66.
49. Pinter M, Jain RK. Targeting the renin-angiotensin system to improve cancer treatment: implications for immunotherapy. Sci Transl Med 2017; 9:eaan5616.
50. Drobni ZD, Michielin O, Quinaglia T, Zlotoff DA, Zubiri L, Gilman HK, et al. Renin–angiotensin–aldosterone system inhibitors and survival in patients with hypertension treated with immune checkpoint inhibitors. Eur J Cancer 2022;163: 108–18.
51. Emblem KE, Gerstner ER, Sorensen G, Rosen BR, Wen PY, Batchelor TT, et al. Abstract 3975: Matrix-depleting anti-hypertensives decompress tumor blood vessels and improve perfusion in patients with glioblastomas receiving anti-angiogenic therapy. Cancer Res 2016;76 (14_Supplement):3975.
52. Mpekris F, Voutouri C, Baish JW, Duda DG, Munn LL, Stylianopoulos T, et al. Combining microenvironment normalization strategies to improve cancer immunotherapy. Proc Natl Acad Sci U S A 2020;117:3728–37.
53. Liu J, Liao S, Diop-Frimpong B, Chen W, Goel S, Naxerova K, et al. TGF-β blockade improves the distribution and efficacy of therapeutics in breast carcinoma by normalizing the tumor stroma. Proc Natl Acad Sci U S A 2012;109:16618–23.
54. Martin JD, Panagi M, Wang C, Khan TT, Martin MR, Voutouri C, et al. Dexamethasone increases cisplatin-loaded nanocarrier delivery and efficacy in metastatic breast cancer by normalizing the tumor microenvironment. ACS Nano 2019;13:6396–408.
55. Zheng X, Fang Z, Liu X, Deng S, Zhou P, Wang X, et al. Increased vessel perfusion predicts the efficacy of immune checkpoint blockade. J Clin Invest 2018;128: 2104–15.

Downloaded from http://aacrjournals.org/clincancerres/article-pdf/28/14/3076/3186259/3076.pdf by guest on 21 September 2023